Received: 31 July 2023 | Revised: 24 December 2023 | Accepted: 7 February 2024

DOI: 10.1002/hsr2.1945

ORIGINAL RESEARCH

Health Science Reports Open Access WILEY

3D bioprinted aged human post-infarct myocardium tissue model

Gozde Basara[1] | Lara Ece Celebi[1,2] | George Ronan[1,2] | Victoria Discua Santos[3] | Pinar Zorlutuna[1,2,4,5]

[1]Department of Aerospace and Mechanical Engineering, University of Notre Dame, Notre Dame, Indiana, USA

[2]Bioengineering Graduate Program, University of Notre Dame, Notre Dame, Indiana, USA

[3]Department of Mathematics, University of Notre Dame, Notre Dame, Indiana, USA

[4]Department of Chemical and Biomolecular Engineering, University of Notre Dame, Notre Dame, Indiana, USA

[5]Harper Cancer Research Institute, University of Notre Dame, Notre Dame, Indiana, USA

Correspondence

Pinar Zorlutuna, University of Notre Dame, 143 Multidisciplinary Research Bldg, Notre Dame, IN 46556, USA.
Email: Pinar.Zorlutuna.1@nd.edu and pzorlutuna@gmail.com

Funding information

National Institutes of Health, Grant/Award Number: 1 R01 HL141909-01A1; National Science Foundation, Grant/Award Number: 1651385

Abstract

Background and Aims: Fibrotic tissue formed after myocardial infarction (MI) can be as detrimental as MI itself. However, current in vitro cardiac fibrosis models fail to recapitulate the complexities of post-MI tissue. Moreover, although MI and subsequent fibrosis is most prominent in the aged population, the field suffers from inadequate aged tissue models. Herein, an aged human post-MI tissue model, representing the native microenvironment weeks after initial infarction, is engineered using three-dimensional bioprinting via creation of individual bioinks to specifically mimic three distinct regions: remote, border, and scar.

Methods: The aged post-MI tissue model is engineered through combination of gelatin methacryloyl, methacrylated hyaluronic acid, aged type I collagen, and photoinitiator at variable concentrations with different cell types, including aged human induced pluripotent stem cell-derived cardiomyocytes, endothelial cells, cardiac fibroblasts, and cardiac myofibroblasts, by introducing a methodology which utilizes three printheads of the bioprinter to model aged myocardium. Then, using cell-specific proteins, the cell types that comprised each region are confirmed using immunofluorescence. Next, the beating characteristics are analyzed. Finally, the engineered aged post-MI tissue model is used as a benchtop platform to assess the therapeutic effects of stem cell-derived extracellular vesicles on the scar region.

Results: As a result, high viability (>74%) was observed in each region of the printed model. Constructs demonstrated functional behavior, exhibiting a beating velocity of 6.7 μm/s and a frequency of 0.3 Hz. Finally, the effectiveness of hiPSC-EV and MSC-EV treatment was assessed. While hiPSC-EV treatment showed no significant changes, MSC-EV treatment notably increased cardiomyocyte beating velocity, frequency, and confluency, suggesting a regenerative potential.

Conclusion: In conclusion, we envision that our approach of modeling post-MI aged myocardium utilizing three printheads of the bioprinter may be utilized for various applications in aged cardiac microenvironment modeling and testing novel therapeutics.

KEYWORDS
3D bioprinting, extracellular vesicles, human induced pluripotent stem cell-derived cardiac fibroblasts, human induced pluripotent stem cell-derived cardiomyocyte, myocardial infarction, post-MI models, therapeutics

1 | INTRODUCTION

Cardiovascular disease (CVD) continues to be the leading cause of death in the world, and is responsible for 2396 average deaths each day in the United States alone.[1] Myocardial infarction (MI) is a type of CVD that arises as a result of atherosclerosis that eventually causes myocardial ischemia, and composes 17% of CVD-related deaths.[1] Immediately after the infarction, most myocardial cells undergo localized necrosis followed by inflammatory, proliferative, and maturation phases of wound healing.[2] During the inflammatory phase, the immune system secretes small proteins such as cytokines and chemokines to clear the infarct area of necrotic cardiomyocytes and extracellular matrix (ECM) debris.[3] Consequently, in the proliferative phase, new muscular tissue forms in the region. In this phase, new tissue begins to develop and myofibroblasts and endothelial cells proliferate into the infarct area.[4] Wound healing concludes in the maturation phase where the newly formed tissue matures and forms a collagenous scar.[2] Unfortunately, this newly formed scar tissue is ultimately detrimental, as it commonly results in arrythmias and eventual heart failure in patients who survived MI initially.[5]

Additionally, aging plays an important role in the onset of MI, with the average age of a patient's first heart attack being 65.6 years for males and 72 years for females.[1] ECM degeneration due to aging is believed to hinder cell functionality, which can increase the risk of MI and other CVDs.[6] Moreover, these age-dependent changes in the heart accentuate the effect of MI, exacerbating the scar tissue formed afterwards.[7] Therefore, it is important to create in vitro models that can recapitulate an aged cardiac microenvironment using aged ECM[8] as well as aged cells,[9] an effort which has recently begun in earnest but has thus far failed to successfully produce such a model.

One of the main challenges in cardiac tissue engineering is the scarcity of disease models that recapitulate post-infarct myocardium.[2,10,11] In vivo models are commonly used to study MI and post-MI tissues because they allow for a whole-body systemic response under pathological conditions.[12–15] However, these models cannot accurately represent human physiological responses due to underlying differences in physiology and anatomy. With the emergence of tissue engineering, post-MI tissue was modeled using different methods, such as microfluidic devices, organoids, and so forth, hydrogels, and cell types to create a more physiologically, biochemically and mechanically relevant post-MI human microenvironment to examine the effect of each contributor.[16–18] Yet, these models fall short in recapitulating the complex microenvironment and the mechanical cues of the native post-infarct myocardium, as well as the effect of age.

The post-infarct myocardial microenvironment can be characterized by a three-part structure: scar tissue, border tissue, and remote healthy tissue, each with distinct mechanical and biological properties such as stiffness and cell composition.[19] Scar tissue is stiffer than the surrounding healthy tissue due to an increase in collagen deposition and crosslinking. Border tissue is slightly stiffer than healthy tissue due to a lower collagen increase compared to scar tissue. Finally, healthy remote tissue has an "average" stiffness, allowing for proper ventricular compliance and diastolic activity.[19]

These differences observed in the native post-MI tissue should be taken into consideration while creating the in vitro tissue models. Although three-dimensional (3D) bioprinting has been widely utilized to recapitulate the complex healthy cardiac microenvironment, there are only a number of 3D bioprinted post-MI tissue models,[18,20–22] and none of them take into consideration the aged microenvironment or cells. Previously, extrusion-based bioprinting has been used for a variety of purposes, from printing entire myocardial constructs, heart valves, and blood vessels,[20] to creating fibrotic tissue models.[21,22] Gelatin methacryloyl (GelMA) hydrogel is commonly used in bioprinting either by itself or combined with other biomaterials[23] as a bioink because of its printability, tunability, and overall cell activity enabling properties.[22,24–26] Methacrylate hyaluronic acid (MeHA) is another biomaterial utilized as a bioink because of its improved mechanical properties and rigidity[27] after being crosslinked, and has also been utilized in conjunction with GelMA due to the biocompatibility of both materials.[28]

Creating a biomimetic post-MI tissue model is important to create platforms to test the efficacy of novel regenerative therapies. Recently, novel regenerative treatments with extracellular vesicles (EVs) have been proven to be effective for the treatment of MI.[29] EVs are common vehicles for transport of both local and systemic communication between tissues, often through transported cytokines, miRNAs, or other small biomolecules.[30] While there are several major categories of EVs, exosomes, those with sizes ranging from 30 to 200 nm, have been increasingly investigated as mediating critical microenvironmental effects in both the onset and resolution of CVDs.[31] In addition to the diagnostic potential of cardiovascular exosomes,[32] recent evidence has suggested that certain populations of exosomes, typically obtained from stem cells, can provide therapeutic effects in damaged heart tissue independently from stem cells themselves.[33] Several preclinical and early clinical trials have investigated the utility of mesenchymal stem cell (MSC) or induced pluripotent stem cell (iPSC)-derived exosomes as a novel, cell-free therapeutic for the treatment of MI or other large heart injury.[34,35] These studies have found that the usage of stem cell exosomes either equals or surpasses treatment outcomes from using

stem cells directly. However, the underlying mechanism and activity of these exosomes in damaged cardiac tissue is not well understood, limiting both the scalability and control over these novel therapeutic strategies.

To bridge the current gap between clinical outcomes and in vitro post-MI tissue models, so as to better inform on responses to regenerative therapies, we 3D bioprinted an aged human post-MI tissue model, including all three regions of the post-infarct microenvironment. In each region, we encapsulated different percentages of cardiac cells; we combined various concentrations of aged human iPSC (hiPSC)-derived cardiomyocytes (iCMs), cardiac fibroblasts (iCFs), endothelial cells (iECs), and cardiac myofibroblasts (iCMFs) with different concentrations of GelMA, MeHA, aged collagen type I, and PI to closely recapitulate the aged post-infarct myocardium in vivo. For that reason, the remote region contained iCMs, iCFs, and iECs, the border region contained iCMFs in addition to the previously mentioned three cell types, and the scar section contained only iCMFs. Although previous studies frequently utilized stem cells to engineer human heart models,[36] either using iCMs alone[37] or in combination with other cell types such as iECs,[13,38–41] iECs and iCFs,[42] or iECs, iCFs and hiPSC derived smooth muscle cells,[43] our study advances the field by engineering a 3D coculture using iCMs, iCFs, iECs and iCMFs to create patient-specific human post-MI tissue models. Moreover, by using aged cells and aged collagen, we introduced the effect of aging in a post-MI tissue model for the first time. Additionally, to accurately mimic the stiffness of each region, we used GelMA, MeHA, and aged human collagen to bioprint the three sections with individual stiffnesses, utilizing a BIOX6 bioprinter. After printing, we assessed cell viability via live/dead staining, and validated cell phenotype and placement by immunofluorescence staining. We then evaluated tissue health and function through beating characteristics, including beating velocity and frequency. Finally, we used the bioprinted aged post-MI tissue model as a benchtop platform to assess the therapeutic effect of either hiPSC-derived EVs (hiPSC-EVs) or MSC-derived EVs (MSC-EVs) by analyzing the beating characteristics.

2 | MATERIALS AND METHODS

2.1 | Cell culture

2.1.1 | hiPSC and MSC culture

The DiPS 1016 SevA hiPSC line derived from human skin fibroblasts (passage number 30–40) was cultured on Geltrex (1% Gibco)-coated tissue culture flasks in mTeSR-1 medium (StemCell Technologies) supplemented with penicillin (Pen) (1%, VWR) at 37°C with 5% CO_2. Around 80% confluency, the hiPSCs were detached from the culture flask using Accutase (StemCell Technologies), and seeded in Geltrex (1%)-coated culture well-plates in mTeSR-1 media supplemented with Rho-associated, coiled-coil containing protein kinase (ROCK) inhibitor (5 μM; StemCell Technologies). The hiPSC culture was maintained with daily media changes with fresh mTeSR-1 until 95% confluency was reached.

MSCs were a kind gift from Dr. Glen Niebur. MSCs were kept in culture in tissue culture flask in DMEM low glucose (1 g/L glucose, Corning), supplemented with 10% exosome-free fetal bovine serum (FBS) and 1% Pen. Media was collected after 48 h in culture post-plating, then successively every 24 h and preserved for EV isolation.

2.1.2 | iCM differentiation induction

A previously established protocol was adapted to induce iCM differentiation.[44] When hiPSCs reached 95% confluency, they were treated with CM (−) (RPMI Medium 1640 (Corning) supplemented with B27 without insulin (2%, Gibco), beta-mercaptoethanol (βME) (final concentration of 0.1 mM, Promega), and Pen (1%) with the addition of Wnt activator, CHIR99021 (CHIR) (10 μM, Stemgent). On Days 2 and 3, the media was replaced with CM (−) containing 2 μM CHIR. On Day 4, iCMs were treated with CM (−) media supplemented with the Wnt inhibitor IWP-4 (5 μM, Stemgent). On Day 6, the media was changed to CM (−). On Day 9, cells were treated with CM (+) (RPMI Medium 1640 supplemented with B27 [2%, Gibco], βME [final concentration of 0.1 mM], and Pen [1%]). After Day 9, cell culture was maintained with media changes using CM (+) every 3 days. As noted in our previous papers, beating of iCMs was often observed by Day 21 of differentiation.[38] To obtain aged iCMs, they were kept in culture for at least 3 months before being used in the experiments. As previous studies from our lab have shown, after 3 months in culture, iCMs display cellular characteristics of aging such as low beating frequency, lipofuscin granule formation and decreased expression of NKX2.5 and ki67 similar to the native cells of aged heart.[9]

2.1.3 | iCF and iCMF differentiation induction

A previously published differentiation protocol was adapted for CF differentiation from hiPSCs.[45] At 100% confluency, hiPSCs were treated with CM (−) supplemented with 10 μM CHIR99021. After 24 h, the media was replaced with CM (−) without CHIR. On Day 3, the media was changed to CFBM media (Supporting Information S1: Table 1) supplemented with FBS (10% Hyclone), containing 75 ng/mL FGF, and this process was repeated every other day until Day 20. On Day 20, the tissue culture flask was coated with fibronectin (Sigma Aldrich) in phosphate-buffered saline (PBS) (50 μg/mL). The iCFs were then detached using trypsin-EDTA (0.25%, Stem Cell Technologies) and passaged on these flasks and cultured in DMEM (Dulbecco's modified Eagle's medium) high glucose media (4.5 g/L, basal medium, Corning) supplemented with FBS (10%), penicillin–streptomycin (P/S, 1%) (Sigma), and SD208 (3 μM, TGF-β receptor 1 kinase inhibitor) (Sigma-Aldrich, St. Louis). iCFs were maintained with media changes with SD208 (3 μM) added DMEM high glucose media supplemented with FBS (10%) and P/S (1%) (DMEM complete) every 2 days and kept at 37°C with 5% CO_2.

After differentiation, the cells were characterized using brightfield imaging, immunofluorescence, and qRT-PCR and successful differentiation was confirmed (Supporting Information: Figure S1). For iCMF differentiation induction, iCFs were treated with DMEM high glucose media supplemented with TGF-β (10 ng/mL, Abcam) when they were around 80% confluency. iCMFs were maintained with media changes using DMEM complete every 2 days and kept at 37˚C with 5% CO_2. The success of the transdifferentiation was confirmed using immunofluorescence-specific markers (Supporting Information: Figure S2).

2.1.4 | iEC differentiation induction

A previously reported differentiation protocol was adapted for cardiac endothelial cell differentiation from hiPSCs.[46] In brief, hiPSCs were treated with a 1:1 mixture of DMEM to F12 with Glutamax and Neurobasal media supplemented with N2 (Life Technologies), B27, CHIR (8 µM), and bone morphogenic protein 4 (25 ng/mL, R&D Systems). After 4 days, the media was changed to StemPro-34 SFM medium (Life Technologies) supplemented with vascular endothelial growth factor (200 ng/mL, PeproTech) and forskolin (2 µM, Sigma-Aldrich), and on Day 5, the media was replaced again. On Day 6, the cells were then sorted against vascular endothelial cadherin (VE-Cad) (Abcam) utilizing magnetic assisted cell sorting (MACS) using an autoMACSpro (Miltenyi Biotec, Harvard University). The purity of the cell population was validated using fluorescence-assisted cell sorting. After higher than 95% purity was ensured, iECs were cultured on fibronectin-coated (50 µg/mL) tissue culture flasks in endothelial growth medium-2 (EGM-2, Lonza).

2.2 | 3D bioprinting the post-MI tissue model

2.2.1 | GelMA and MeHA synthesis

To synthesize the photocrosslinkable GelMA and MeHA hydrogels, previously established protocols were utilized.[47,48] In brief, 10 g of gelatin (gel strength 300 g Bloom, Type A, from porcine skin, Sigma-Aldrich) was dissolved in 100 mL of PBS at 60°C. Then, 2 mL of methacrylic anhydride (Manh, Sigma-Aldrich) was added dropwise slowly while keeping the pH around 8 and constantly stirring at 60°C. After 3 h, the solution was diluted with 400 mL of PBS at 40–50°C and stirred. After 15 min, the solution was transferred into 12–14 kDa MWCO dialysis membranes (VWR) and dialyzed against DI water for a week with twice-daily water changes. Lastly, the GelMA solution was filtered and lyophilized for further use. MeHA was obtained by dissolving 0.2 g of HA (MW: 1.5–1.8 × 10^6 Da, Sigma-Aldrich) in 60 mL DI water at room temperature with constant stirring. After 24 h, 40 mL dimethylformamide (DMF, Sigma-Aldrich) was added dropwise using a glass pipette. Then, 0.8 mL of Manh was added dropwise and the pH was adjusted to 8–9 for the reaction to take place at 4°C. The following day, the mixture was placed in 12–14 kDa MWCO dialysis membranes and dialyzed against DI water. After 3 days, the water is replaced 2–3 times a day before filtering and lyophilizing. Finally, the degree of methacrylation was quantified using NMR (Supporting Information: Figure S3).

TABLE 1 Final concentrations of hydrogel components used in remote, border and scar regions.

	GelMA	MeHA	Collagen (mg/mL)	PI (%)
Remote	10% w/v	-	1	0.025
Border	12% w/v	-	1.5	0.033
Scar	15% w/v	1% w/v	2	0.15

2.2.2 | Mechanical characterization of the Bioinks

The hydrogels used to create the different regions: remote (healthy), border and scar (infarct) of the post-MI tissue model, were prepared with the concentrations reported in Table 1. First, GelMA was dissolved in PBS at the required concentrations and the mixture was kept in a water bath at 37°C until the solution was completely homogeneous. Then, MeHA was dissolved in PBS to obtain 3% (w/v) and the mixture was kept at 80°C for 1 h, until the MeHA was completely dissolved. Aged collagen type 1 (6 mg/mL) (HumaBiologics) was titrated to adjust the pH to 7 and kept at 4°C before mixing. Irgacure2959 photoinitiator (PI, Sigma) solution was prepared (1% w/v in PBS) and was added to GelMA and MeHA solutions using the concentrations given in Table 1. Then, collagen was added to the mixture in the desired concentration, and the solution was transferred onto a stage with 100-µm-thick spacers and sandwiched between the stage and a glass slide. The Young's modulus of each of the prepared bioinks was measured by performing compression tests using a nanoindenter (Optics 11) with an indentation probe (spring constant of 0.51 N/m, tip diameter of 46 µm) as reported previously.[22] Then, the Young's modulus of each of the bioinks was determined by calculating the slope of the stress–strain curve in the elastic region, which was obtained using an in-house MATLAB code.

2.2.3 | Bioprinting the post-MI tissue model

To engineer a biomimetic post-MI tissue model, bioinks were prepared by combining different concentrations and combinations of cells and hydrogels to mimic a real post-infarct region. Aged iCMs (>3 months), high-passage iCFs (passage 9–14), high-passage iECs (passage 9–14), and high-passage iCMFs (passage 9–14) were detached using trypsin-EDTA. After centrifugation at 1000 rpm for 5 min, cell combinations and concentrations were combined together so that each tube has the required cell type and amount to represent each region as presented in Table 2 and centrifuged again. After removing the supernatant, each cell combination was mixed with the corresponding hydrogel solution shown in Table 1. This was done by

resuspending the resultant cell pellet in the required volume of collagen necessary to construct each gel, then mixing the cell-collagen solution with the prepared hydrogel, sans collagen, solution. Bioinks representing the different regions were placed in individual cartridges and submerged in an ice bath for 1–2 min to achieve the necessary consistency for printing.

CELLINK BioX6 Bioprinter (CELLINK) and a custom-made G-Code were used to print the post-MI tissue model. Three printheads with 22G nozzles were employed and three concentric circles with reported dimensions (Table 3) were printed on a sterilized charged glass (Globe Scientific Inc.) placed in a 60-mm dish. This process was carried out using a translational speed of 3.5 mm/s. Immediately after printing, the constructs were photocrosslinked with 30 s UV (6.9 W/cm^2 UV radiation) using a UV lamp (Lumen Dynamics). Printed constructs were then placed in a well-plate with 1 mL of DMEM complete and media was changed three times every 10 min, for a total of 30 min. Finally, the media was replaced with a combination media made of equal volumes of CM (+) for the nourishment of iCMs, EGM-2 for the nourishment of iECs and DMEM high glucose media (4.5 g/L, basal medium) supplemented with 3 μM SD208 for the nourishment of iCFs in the construct.

2.3 | Characterization of the tissue constructs

2.3.1 | Cell type characterization of the post-MI tissue model

Differentiated cells were collected using trypsin-EDTA and tagged with cell trackers before printing. iCMs were tagged with CellTracker green CMFDA (1 μM, Life Technologies), iCFs were tagged with CellTracker blue (1 μM, Life Technologies), iECs were tagged with CellTracker orange CMTMR (1 μM, Life Technologies), and iCMFs were tagged with CellTracker deep red (1 μM, Life Technologies) dyes following the manufacturer's instructions. After printing, the tiles images were taken and stitched together using a fluorescence microscope (Zeiss, Hamamatsu ORCA flash 4.0).

TABLE 2 Cell composition of remote, border, and scar regions.

	iCMs (mil/mL)	iCFs (mil/mL)	iECs (mil/mL)	iCMFs (mil/mL)
Remote	20	6	3	-
Border	10	3	1.5	1
Scar	-	-	-	10

2.3.2 | Cell viability characterization of the post-MI tissue models

To evaluate the viability of the 3D printed post-MI tissue models, live/dead assay was performed (Life Technologies) following the manufacturer's instructions. Briefly, 24 h after the printing, the constructs were washed twice using PBS and incubated in a solution containing calcein AM (live cells, green, 2 μM), Ethidium homodimer-1 (dead cells, red, 4 μM), and Hoescht (8 μM, Thermo Scientific) at 37°C about 30 min. Then, for every sample, z-serial images were taken with the confocal microscope. Finally, live and dead cells were counted using a custom MATLAB code and viability percentage was quantified by using the following equation:

$$\text{live cell (\%)} = [(\text{live cell number})/(\text{total cell number})] \times 100. \quad (1)$$

2.3.3 | Immunostaining

Immunostaining was performed on the constructs to show the cell-specific protein expression in different regions, as well as to analyze the cell–cell and cell–matrix-related protein expressions. Briefly, 7 days after the printing, the constructs were washed twice using PBS and fixed using paraformaldehyde (4%, Electron Microscopy Sciences) for 1 h for at room temperature, and then washed with PBS for 30 min with washes every 10 min. Cells were permeabilized by incubation in Triton X-100 (0.1%, Amresco) solution for 45 min and then washed with PBS three times every 10 min, in total 30 min. Then, goat serum (10%, Sigma-Aldrich) was used to block the cells for 2 h at room temperature, and cells were incubated with desired primary antibody diluted according to the manufacturer's recommendations (Supporting Information: Table 2) at 4°C overnight. Constructs were then washed with PBS, and incubated with secondary antibodies, 647-rabbit (Abcam) and 488-mouse (Abcam), diluted (1:200) in goat serum at 4°C for 6 h. Constructs were then washed with PBS three times and incubated with DAPI (1 μg/mL w/v in PBS, Sigma Aldrich) for 5 min at room temperature. The washing process with PBS was repeated until no background remained. Before imaging, constructs were mounted using Prolong gold (Invitrogen).

TABLE 3 Printing parameters and construct dimensions.

Printer type	Nozzle size	Printing speed	Printing pressure	Temperature	Construct diameters
CELLINK BioX6 Bioprinter	22G (410 μm)	3.5 mm/s	10–15 kPa	Room temperature (25–30°C)	Remote (hollow cylinder): 10 mm outer diameter, 6 mm inner diameter, 0.3 mm height Border (hollow cylinder): 6 mm outer diameter, 4 mm inner diameter, 0.3 mm height Scar (cylinder): 4 mm diameter, 0.3 mm height

Finally, imaging was performed with airyscan and fluorescence microscopy. Post imaging processing was performed using the Zeiss Zen software and ImageJ (National Institutes of Health).

2.3.4 | Beating analysis

To analyze the beating characteristics of iCMs in the post-MI tissue model, 20 s bright field videos at ×20 magnification were taken on Day 1 and Day 3 after printing. Then, the beating velocity and frequency of the printed constructs were quantified. Video analysis of lateral displacement of spontaneous beating iCMs and heat maps were generated using an in-house MATLAB code as previously described.[22]

2.4 | Stem cell-derived EVs treatment

2.4.1 | Vesicle isolation

Supernatant was collected from SEVA iPSC, or MSC cultures after 48 h in culture post-plating, and then every 24 h. Collected media was centrifuged three times successively at 500*g* for 10 min, 2500*g* for 20 min, and 10,000*g* for 30 min to remove dead cells or other debris from the supernatant. The purified supernatant was then ultracentrifuged at 100,000*g* for 70 min at 4°C to obtain an exosome pellet. The remaining supernatant was removed, and the pellet was either used immediately or stored at −80°C.

2.4.2 | Vesicle staining

EVs were stained with the ExoGlow (System Biosciences) kit, according to the manufacturer's protocol. Briefly, EV content was quantified using bicinchoninic acid gold protein quantification assay (Thermo Fisher Scientific), and 100 µg of the sample was resuspended in 12 µL of provided reaction buffer. Next, 2 µL of ExoGlow stain was added and the solution was mixed, allowing the reaction to take place for 30 min at room temperature in the dark. The stained EVs were then isolated using a density gradient column (GE Healthcare) and resuspended in 1 mL of PBS. Stained EVs were then isolated from the solution by ultracentrifugation at 100,000*g* for 70 min at 4°C and immediately resuspended in 30 µL of PBS for direct injection. To prepare hydrogel–EV mixtures, EVs were combined with shear thinning hydrogel solution consisting of 3% gelatin (w/v PBS) and 4% microbial transglutaminase (w/v PBS). They were then injected into the scar zone of the models and kept at room temperature for 5 min allowing the hydrogel to crosslink before placing the media. 3D bioprinted tissue models were treated with either only EVs or EV–hydrogel mixture for 3 days. On Day 1 and Day 3, brightfield videos were taken and beating velocity and frequency were analyzed as described in the previous section. Additionally, beating confluency analysis was conducted, revealing the ratio of beating area over total area covered by the cells. Immediately after taking videos on Day 3, the models were fixed and stained using CD9 antibody (1:100, Abcam), and VE-Cadherin (1:100, Abcam), following the manufacturer's protocol and the methodology described above. Before imaging, samples were mounted using Prolong gold. Then, imaging was performed with airyscan and fluorescence microscopy. Finally, Zeiss Zen software and ImageJ were employed for post imaging processing.

2.5 | Statistical analysis

Data were represented as average ± standard deviation or average ± standard error of the mean (SEM), when specified. The one-way analysis of variance (ANOVA) with Tukey's post hoc was used to find any statistically significant differences. If there were two individual groups, the Student's *t*-test was performed. All *p* values were reported to be two-sided, and $p < 0.05$ was considered statistically significant. Sample size (n) ≥3 for all individual experiments.

3 | RESULTS

3.1 | 3D bioprinting the aged human post-MI tissue model

Post-MI myocardium undergoes biomolecular and biomechanical changes over time.[2] In this study we created an in vitro model representing the maturation phase post-MI (weeks or months after MI), which can be characterized by three distinct regions: remote, border, and scar, represented here as red, yellow, and grey respectively (Figure 1A). Previous in vivo studies report that the scar region is vastly different in terms of stiffness, collagen concentrations and cell types compared to the border and the remote regions.[49] To account for these variations, bioinks were prepared combining GelMA, collagen, and MeHA in various concentrations and by mixing them with the required cell types to closely mimic the in vivo construction of each region, as described in the previous section. The hydrogels were combined such that final concentrations of 10% GelMA, 1 mg/mL collagen, 0.025% PI for remote, 12% GelMA, 1.5 mg/mL collagen, 0.033% PI for border, and 15% GelMA, 1% MeHA, 2 mg/mL collagen, 0.15% PI for scar region are obtained. The Young's modulus of each of the prepared composite hydrogels was measured to be 1.5 ± 0.7 kPa for remote, 2.0 ± 0.8 kPa for border, and 10.9 ± 1.6 kPa for scar, demonstrating the desired change in the stiffness as expected from the manipulation of collagen and hyaluronic acid concentrations (Figure 1B).

To show the different cell types and concentrations in each region, cells were stained using a cell tracker before printing (Figure 1C). The scar region is populated with only iCMFs (deep red); the border region is populated with all cell types: iCMFs, iCFs (blue), iECs (orange), and iCMs (green); and the remote region is greatly populated with iCMs as well as iCFs and iECs.

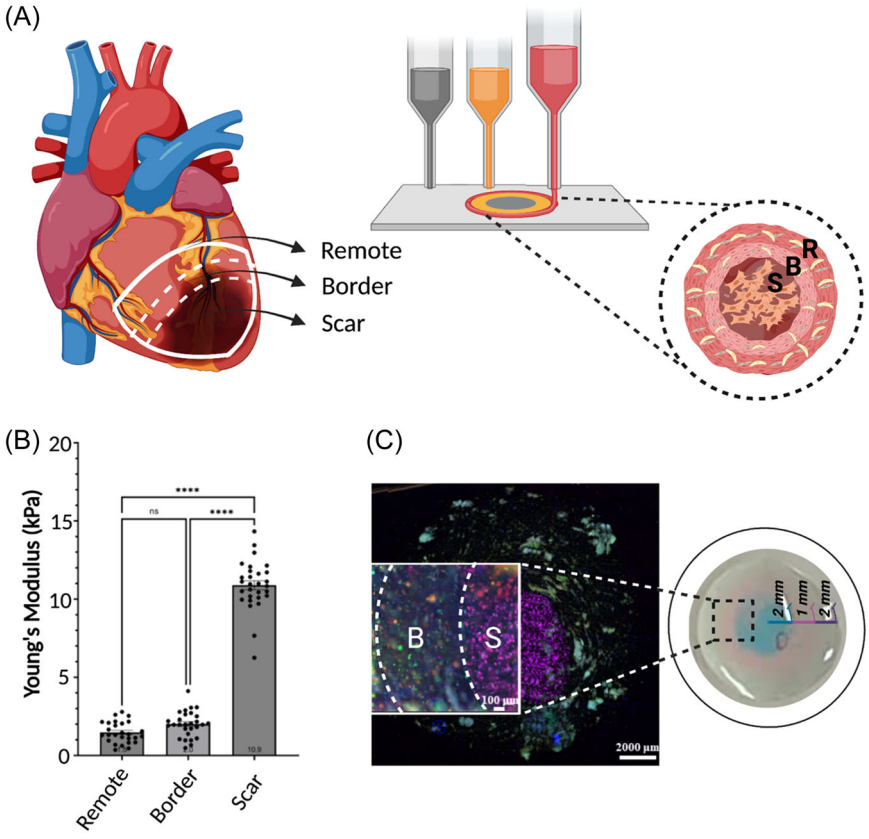

FIGURE 1 Three-dimensional bioprinting of the post-myocardial infarction (MI) tissue model. (A) Schematic showing the three regions formed post-MI (R: Remote, B: border, S: scar). (B) Young's Modulus results of the composite hydrogels representing each region. (C) Tiles image showing the printed post-MI model after staining the cells using cell tracker (human iPSC-derived cardiomyocytes [iCMs] were tagged with CellTracker green, hiPSC-derived cardiac fibroblasts [iCFs] were tagged with CellTracker blue, hiPSC-derived endothelial cells [iECs] were tagged with CellTracker orange, and hiPSC-derived cardiac myofibroblast [iCMFs] were tagged with CellTracker deep red). The inset is showing the zoomed in image ($n = 3$, n.s.: nonsignificant, ****$p < 0.0001$).

3.2 | Viability assessment of the 3D bioprinted aged human post-MI tissue models

The effect of different hydrogels, PI concentrations, and bioprinting process on the viability of the cells was evaluated by performing live/dead staining 24 h post-printing (Figure 2). The images were taken using confocal microscopy and the viability percentage of each region was calculated to be 83% ± 8% for the remote region (Figure 2B), 75% ± 14% for the scar region (Figure 2C), and 75% ± 12% for the border region (Figure 2D), respectively.

3.3 | Immunofluorescence characterization of the 3D bioprinted aged human post-MI tissue models

In the printed post-MI tissue model, each region consists of combination of different cell types and hydrogels. To show the specific characteristics of the cells forming each region, immunofluorescence staining was performed 7 days after printing, using cell-specific proteins. The remote region was comprised of iCMs, iCFs, and iECs; therefore, cell-specific proteins such as sarcomeric alpha actinin [SAA] (for iCMs), Vimentin (for iCFs), and VE-Cadherin (for iECs) were used (Figure 3A). The border region included all the cell types exists in the remote region with the addition of iCMFs, which was stained with myofibroblast marker alpha smooth muscle actin [α-SMA] (Figure 3B). The scar region consisted of only iCMFs, and therefore was stained only with Vimentin and α-SMA (Figure 3C). Each region was also stained using Vinculin and N-Cadherin to identify the changes in cell–cell and cell–matrix interactions resulting from the changing hydrogel and cell concentrations. The expressions of Vinculin and N-Cadherin in the remote and border regions were normalized to cell number and, the Vinculin and N-Cadherin expressions at the scar region. The fold change for Vinculin expression was calculated as 0.45 ± 0.20 (SEM) and 0.73 ± 0.17 (SEM), for the remote and border regions, respectively (Figure 3D). For N-Cadherin the fold change was 0.53 ± 0.22 (SEM) for the remote region and the border region was 0.69 ± 0.16 (SEM) (Figure 3E).

3.4 | Beating characteristics of the printed post-MI tissue models

As early as 24 h after printing, spontaneous beating was observed in the remote and border regions. On Day 1 and Day 3 following printing, brightfield videos were taken to observe the beating characteristics of the iCMs in the remote region. Beating velocity and frequency were calculated using an in-house MATLAB code with the block-matching algorithm as explained in detailed previously[50] and heat maps were generated for confluency calculation in addition to beating velocity and frequency (Figure 4A,B). While beating velocity indicates the rate of change of the CMs' position with respect to time, beating frequency indicates the rate at which beating occurs. Beating velocity was measured to be 5.4± 1.3 µm/s for Day 1

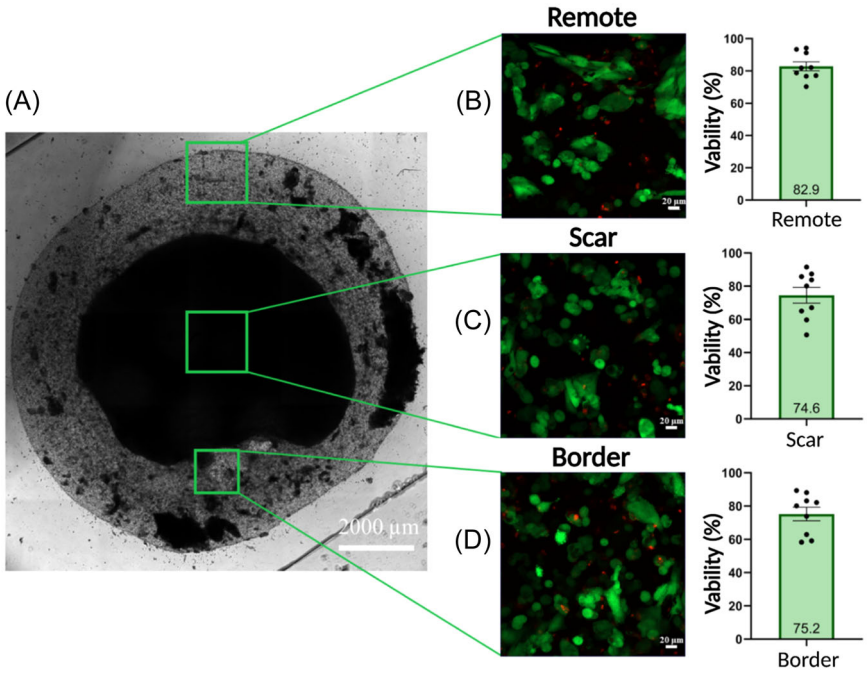

FIGURE 2 Viability assessment for the three-dimensional bioprinted post-myocardial infarction (MI) tissue model with live (green)/dead (red) staining. (A) Brightfield image showing the different regions of the bioprinted construct. Confocal image and viability analysis for (B) remote region (human iPSC-derived cardiomyocytes [iCMs], hiPSC-derived cardiac fibroblasts [iCFs], hiPSC-derived endothelial cells [iECs]), (C) scar region (hiPSC-derived cardiac myofibroblast [iCMFs]), and (D) border region (iCMs, iCFs, iECs, iCMFs) ($n = 3$).

and 6.7 ± 3.5 µm/s for Day 3 (Figure 4C) and beating frequency was calculated as 0.25 ± 0.10 Hz for Day 1 and 0.29± 0.13 Hz for Day 3 (Figure 4D).

3.5 | Using the 3D bioprinted aged human post-MI tissue model as an EV treatment testing platform

After the viability and the functionality of the bioprinted aged human post-MI model was confirmed, it was used as a platform to test the efficiency of hiPSC-EVs, which is among other stem-cell derived EVs that have been investigated for use in post-MI treatments of the scar region.[51–53] Ergo, 3 days after printing the hiPSC-EVs, were either injected directly into the scar region or mixed with a hydrogel before injection. When the EV–hydrogel mixture was injected, EVs were observed to be immobile within the hydrogel and thus stayed in the scar region. This was confirmed via staining for CD9, a well-established EV marker, shown in violet and indicated with white arrows in Figure 5A. Moreover, 3 days after EV treatment, the scar region demonstrated VE-Cadherin expression, which is not observed in cardiac myofibroblasts and specific to endothelial cells[54] (Figure 5B). Similar to Section 3.4, beating velocity and frequency of the nontreated, directly EV-treated, and EV-hydrogel-treated post-MI models were analyzed. When treated with hiPSC-EVs, no significant changes of beating velocity and frequency were observed during the timeframe of this experiment (Supporting Information: Figure S4). When the aged post-MI tissue models were treated with MSC-EVs and the beating velocities of treated models were normalized to nontreated models, the ratio of beating velocities was calculated as 0.86 ± 0.08 for baseline, 1.29 ± 0.43 for Day 1, and 1.40 ± 0.09 for Day 3, revealing a significant increase from baseline to Day 3 (Figure 5C). Similarly, the normalized beating frequencies were quantified to be 0.96 ± 0.05 for baseline, 1.21 ± 0.08 for Day 1, and 1.14 ± 0.06 for Day 3, indicating a significant increase between both Day 1 and Day 3 compared to the baseline values (Figure 5D). Finally, the normalized beating confluency values, which indicates the area occupied by beating CMs, were calculated as 0.92 ± 0.02 for baseline, 1.54 ± 0.57 for Day 1, and 3.99 ± 1.11 for Day 3, revealing a significant increase from baseline to Day 3 (Figure 5E).

4 | DISCUSSION

Although MI remains one of the most common CVDs affecting millions of people worldwide, it is known that scar tissue formed following the MI is an equally lethal contributor. Yet, in vitro platforms to evaluate the efficacy of novel therapies continue to bottleneck research, and animal studies, which requires interspecies translation of the results, are driving much of the advancement in this area.[10,11] Unfortunately, the fundamental differences between animal and human pathology and physiology hinder the successful translation of the results observed in in vivo studies. To advance the field of cardiac tissue engineering, more biomimetic human tissue models are needed. Additionally, the effects of aging have been increasingly investigated in engineered tissue models, due to the difficulty of modeling aging-related changes in animal models and the known relationship between age and clinical outcomes for MI, fibrosis, and other CVDs. This gap in translatable knowledge is a critical junction which necessitates the development of models which can accurately replicate the tissue microenvironment, and mechanical cues which affect tissue behavior and drug response in older individuals.

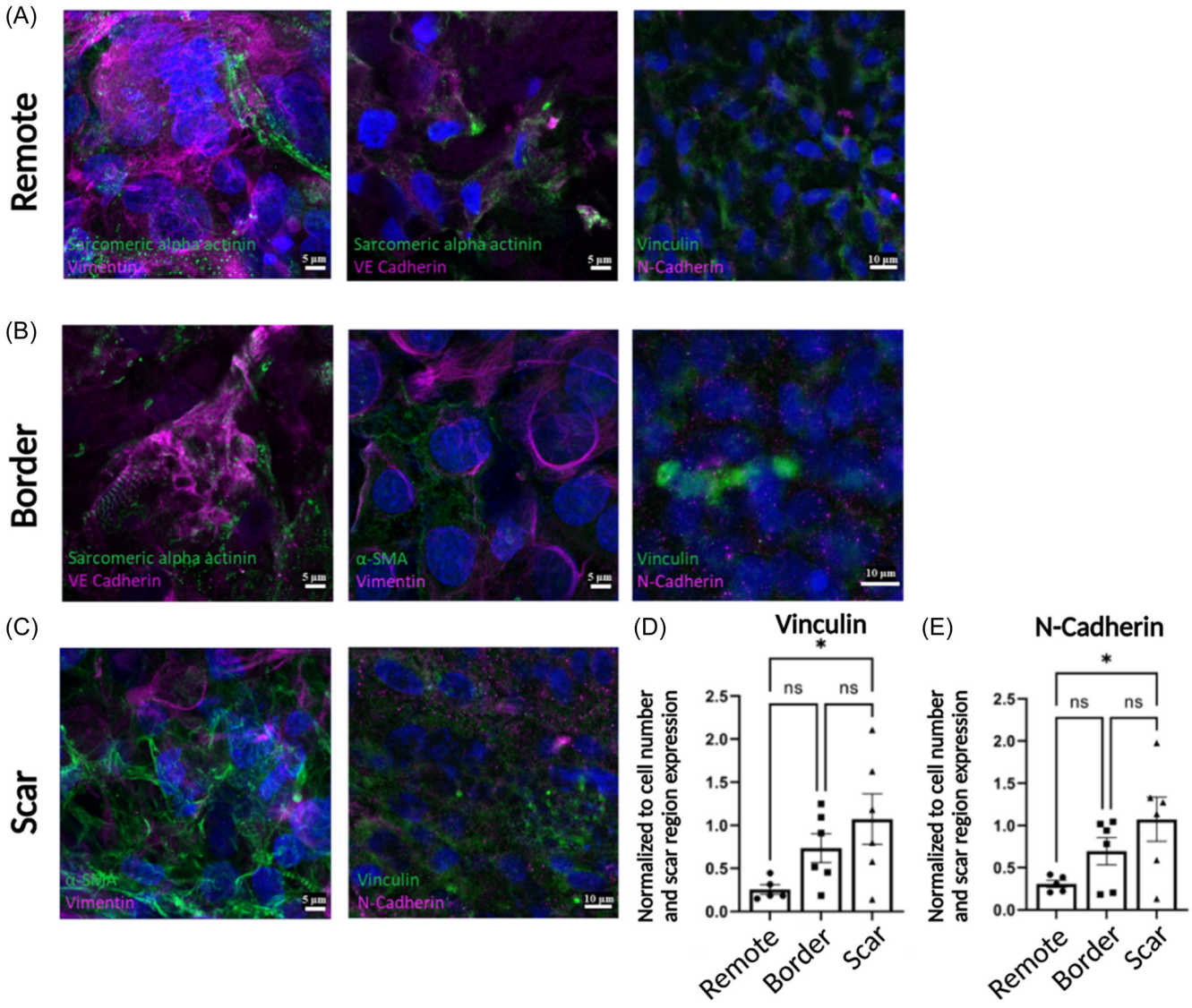

FIGURE 3 Phenotypal characterization of the three-dimensional bioprinted post-myocardial infarction (MI) tissue model. (A) Airyscan images of the remote region showing sarcomeric alpha actinin (SAA) (green), Vimentin (violet) (left image), SAA (green), VE-Cadherin (violet) (middle image), Vinculin (green) and N-Cadherin (violet) (right image), and DAPI (blue) (all). (B) Airyscan images of the border region showing SAA (green), VE-Cadherin (violet), (left image), Alpha smooth muscle actin (α-SMA) (green), Vimentin (violet) (middle image), Vinculin (green) and N-Cadherin (violet) (right image), and DAPI (blue) (all). (C) Airyscan images of the scar region showing α-SMA (green), Vimentin (violet) (left image), Vinculin (green) and N-Cadherin (violet) (right image), and DAPI (blue) (all). (D) Vinculin expression in the remote, border, and scar regions normalized to DAPI and scar region, and (E) N-Cadherin expression in the remote, border, and scar regions normalized to DAPI and scar region ($n = 6$, n.s.: nonsignificant, $^*p < 0.05$) (error bars represent standard error of the mean [SEM]).

Previous in vitro studies are mostly dedicated to developing cardiac tissue models and subsequently inducing hypoxic conditions to create the MI-mimicking conditions,[2,40] and rarely divert any focus to modeling the post-infarct myocardial tissue. A handful of studies developed post-MI tissue models using a microfluidic device,[10,55] whereas some others created an oxygen gradient in the tissue model.[56] Additionally, to mimic the complexity of the post-MI tissue, 3D bioprinting has also been utilized previously.[21] In their study, Koti et al., combined GelMA with rat CMs and rat CFs to represent the healthy and scar region, respectively, and printed using two printheads. Similarly, in our previous study, we engineered a healthy and scar tissue model using two printheads, except we took into consideration the stiffness difference between the healthy and scar regions.[22] Yet, a 3D bioprinted model that combines the mechanical, biomolecular, and cellular difference between the three distinct regions of the post-MI tissue remains to be developed.

In this study, we advanced the field by developing an aged human post-MI tissue model using three different bioinks consisting of various concentrations of GelMA, MeHA, aged collagen, and PI, and four different iPSC-derived aged cardiac cells combined to closely recapitulate the native post-MI tissue formation, using a 3D bioprinter. This is the first study which accomplishes the 3D

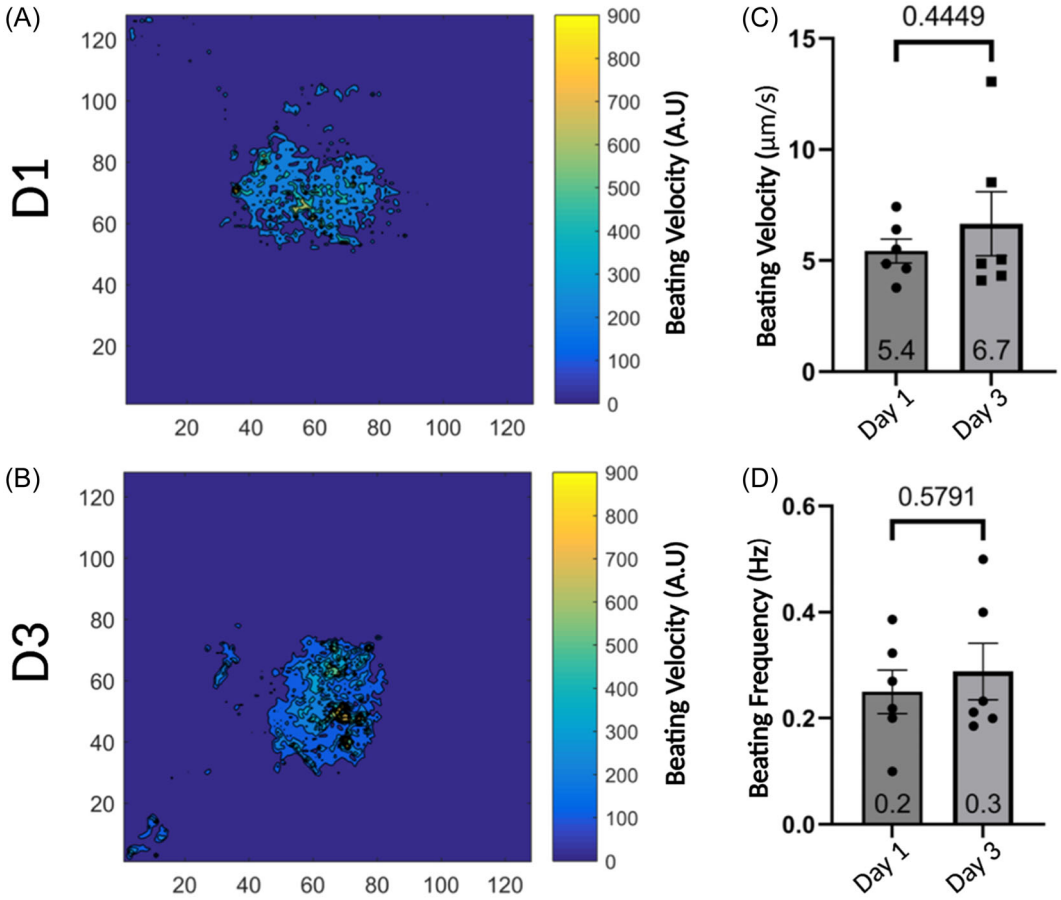

FIGURE 4 Beating characteristics of the remote region of the three-dimensional bioprinted post-myocardial infarction (MI) tissue model. The heat maps showing the beating velocity magnitude (A.U.) and distribution of human iPSC-derived cardiomyocytes (iCMs) encapsulated in the remote region (A) 1 day post printing, (B) 3 days after printing, (C) average beating velocity of the iCMs, and (D) average beating frequency of the iCMs.

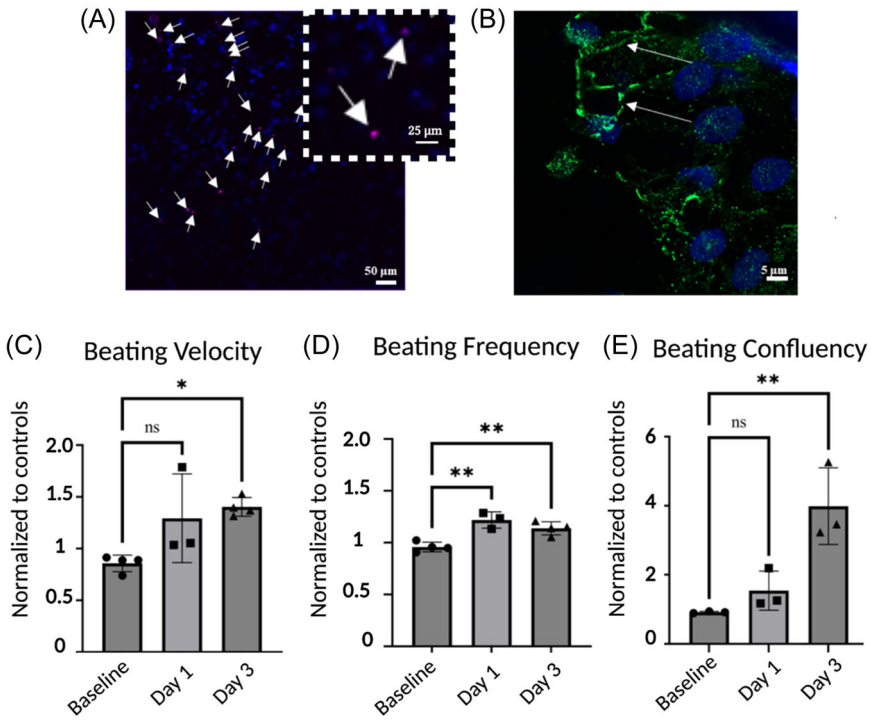

FIGURE 5 Using the three-dimensional bioprinted post-myocardial infarction (MI) tissue model as a platform to test extracellular vesicle (EV) therapy. (A) Fluorescence image showing the CD9-positive EVs (violet) (white arrows pointing the CD9 expression) stayed in the injected scar region when mixed with shear thinning hydrogel. Cell nuclei are indicated with DAPI (blue). (B) VE-Cadherin (green) expression was observed in the EV-treated scar region. (C) Beating velocity of EV-treated post-MI tissue models normalized to the untreated controls each day. (D) Beating frequency of EV-treated post-MI tissue models normalized to the untreated controls each day. (E) Beating confluency percentage of EV-treated post-MI tissue models normalized to the untreated controls each day ($n \geq 3$, n.s., nonsignificant, $^{*}p < 0.05$, $^{**}p < 0.01$).

bioprinting of a post-MI tissue model while accounting for both the biomolecular and biomechanical changes in the in vivo post-MI infarct region. Moreover, while engineering our model, we used hiPSC-derived cardiac cells which can transfer the genetic variations, enabling the creation of patient-specific post-MI tissue models in the future.[37]

In this paper, we have combined various cell types with different hydrogels before printing to engineer three distinct regions and reported high viability (>74% in each region) (Figure 2B–D), which is typically difficult to achieve in photocrosslinked hydrogels due to the adverse effects of Irgacure 2959 PI on cell viability.[57] Here, using a lower PI concentration in the remote and border regions served the dual purpose of decreasing stiffness and enhancing overall cell viability. Due to the increased resilience and survivability of CMFs,[58] increasing the PI concentration to obtain the desired stiffness in the scar region had notably less impact on cell viability than would be expected in other cell types. While it is possible that the viability of the scar region would have been greater if a lower concentration of PI was used, since it has been previously shown that increasing Irgacure 2959 PI concentration has an adverse effect on the cell viability,[59] to have bioinks with the required stiffness it was necessary to use a relatively higher PI concentration.

The utilized printing methodology included different concentrations and types of biomaterials and cells to be printed as three distinct regions. Aged collagen and cells were used to recapitulate the aged cardiac microenvironment. To the best of our knowledge, this is the first study to utilize three printheads and prepare bioinks with four different cell types of myocardium to create an aged human post-MI tissue model. We developed a methodology as explained in detail in the "Materials and Methods" section, which can be employed for many different healthy and diseased tissue modeling applications. In this study, the specific concentrations of the hydrogels forming the different regions were determined considering the mechanical, chemical, and printability characteristics of the bioinks (Figure 1). Keeping these three pillars in mind, the hydrogel concentrations were optimized, and resulted in almost an order of magnitude stiffness difference between the scar region compared to the border and remote regions as shown previously in a large animal model.[49] Moreover, the concentration of collagen and hyaluronic acid has been previously shown to increase in the scar region, which we took into consideration in our model.[49,60] Additionally, the cell concentrations were also determined such that it recapitulate the in vivo post-infarct myocardium tissue.[19,61–63] Finally, the shape of the bioprinted construct was chosen such that it closely resembles the cross-section of the in vivo post-infarct myocardium tissue.[64]

Development of functional tissue constructs via printing is also paramount. Here, the 3D printed models showed a beating velocity of 6.7 μm/s and a frequency of 0.3 Hz on Day 3. Previously our group reported a slightly higher beating velocity (~8 μm/s) and greater frequency (~0.6 Hz) of the 3D bioprinted iCMs alone with GelMA. The decrease in the beating velocity and frequency can be explained by the inclusion of other cell types, which is consistent with the previous studies which reported that the best mechanical performance was achieved with 100% cardiomyocytes compared to 70% and 30% CMs, with the extraneous cells being ECs and CFs, analogous to our study.[65] Another reason for the slightly lower beating performance of our 3D printed models may be the existence of the border and scar regions, and the inclusion CMFs which are known to promote hypertrophy, via release of profibrotic factors,[66] and be otherwise deleterious to healthy myocardium. Additionally, mechanical signals from CMFs previously have shown to affect the electrophysiology of the CMs and decrease the conduction velocity.[67]

To perform a phenotypal characterization of the 3D printed post-infarct myocardium model, we stained all the regions using cell-specific antibodies (Figure 3). Cardiomyocytes were stained with SAA, which is an actin-binding protein bounded at the Z-disks sustaining the muscle contraction.[68] Striated sarcomeres were observed at the remote and border regions where the iCMs were encapsulated (Figure 3A, middle and B, left). To characterize the iECs, VE-Cadherin was chosen as it is specific to endothelial cells.[69] Similar to iCMs, VE-Cadherin expression was observed in the remote and border regions. Vimentin was used as the biomarker for iCFs since it is the most specific marker for them.[70] Vimentin expression was observed in all the regions as the border and remote regions contain iCFs and the scar region consists of iCMFs. Finally, α-SMA, which is a marker for cardiac myofibroblasts,[71] was expressed in both border and scar regions as they contain iCMFs. As shown in Figure 3C, the expression of α-SMA in the scar region is substantially greater than the Vimentin expression, confirming that the cells are cardiac myofibroblasts. These are all well-known markers specific to each cell type, validating that the 3D bioprinted post-infarct myocardium tissue model is closely recapitulating the in vivo post-MI tissue in the maturation phase. After phenotypically characterizing each region, the cell–cell and cell–matrix relations were investigated by staining each region using N-cadherin and Vinculin, respectively. The scar region showed the greatest expression for Vinculin and N-Cadherin, which was in line with the previous literature reporting that increased substrate stiffness would increase both Vinculin and N-Cadherin protein expression.[72,73]

Finally, as a proof of concept, we utilized the developed aged post-MI tissue model as a testing platform for therapeutic strategies. Recently, stem cells and stem-cell-derived EV treatments have shown to improve cardiac functionality post-MI, reduce the infarct region size, and promote angiogenesis.[35] EVs are promising therapeutics, and they present a cell-free biological that can facilitate many of the observed benefits of stem cell therapy. In this study, to maintain the human origin, as well as provide precedent for the use of patient-specific EVs with this model, we first used hiPSC-EVs. We were able to show that EVs stayed in the scar region when we mixed EVs with a hydrogel before injection (Figure 5A). Here, we utilized a shear-thinning hydrogel to ease the injection and subsequent crosslinking independently, which is similar to the HA-based hydrogel that was used previously to create and inject EV mixture into a rat model, and reported that treatment with EVs improved the vessel formation organization.[74] Similarly, after treating with EVs, we observed VE-Cadherin expression at the scar region, where there were initially no endothelial cells encapsulated (Figure 5B), which suggests that the EV

treatment may have independently promoted endothelial cell infiltration and neovascularization. Although previous hiPSC-EV treatment studies reported that EV treatments enhanced the cardiac functionality in vivo[52] we did not observe any significant increase in the beating velocity and frequency of the iCMs forming the remote region as a result of a 3-day treatment. This might be due to longer treatment durations in vivo (around 3 weeks), and the lack of a systematic, whole-body response in this model. On the other hand, we did observe that direct injection of MSC-EVs into the scar region resulted in significant improvement of beating velocity, frequency, and confluency compared to the baseline when normalized to nontreated controls (Figure 5C–E). Our results are in alignment with the previous literature, as MSC-EVs are one of the most commonly used EVs that have been recently gaining popularity as a regenerative therapy due to promising preclinical and clinical results.[51] Additionally, as the post-MI tissue causes arrhythmia, and this effect intensifies in the aged population, showing that the MSC-EV-treated aged human post-MI tissue constructs have improved cardiac function is a promising observation both in the sense of the effectiveness of the developed platform as well as the therapeutic effect of the MSC-EVs.

In this study, we characterized changes in cardiac function by examining beating velocity, frequency, and confluency. In addition to these parameters, previous studies investigated the effect of regenerative treatments on the beating force,[75] displacement[76] and relaxation time,[77] which can be further assessed using our 3D printed post-MI tissue model. To improve the regenerative effect, increasing the EV concentration as well as increasing the treatment duration might be a starting point for future studies. Additionally, beyond testing the therapeutic effect of EVs, the post-MI tissue model developed in this study can be used as a highly controlled platform to better isolate and quantify the effect of age and gender, which have been shown to play a critical role in characteristics and activity of EVs in the cardiac microenvironment specifically in relation to the onset of inflammation and onset of fibrosis.[78]

5 | CONCLUSION

In this study, we 3D bioprinted aged human post-MI tissue models by utilizing three printheads to print three different regions of post infarct myocardium tissue. The hydrogels and cell types for each region were specifically and carefully selected to create a greatly similar tissue model mimicking the native post-MI tissue biomechanically and bimolecularly. As a proof of concept, we showed that these tissue models can be used as platforms to test the therapeutic effect of EVs, demonstrating the potential application of them as a platform for testing novel regenerative therapies before animal studies. We also took into consideration the age factor by using aged cells and collagen, hence allowing the possibility of using these printed tissue models to test the effect of new therapies on different ages.

In conclusion, the 3D bioprinted aged human post-MI tissue models can be used not only to create more biomimetic in vitro models allowing the researchers to test new therapies in vitro on patient-specific tissue constructs but also enable the creation of age-specific models which is a known factor that is affecting the efficacy of the therapies. By better mimicking the native post-MI tissue, these models serve as the much needed bridge between 2D in vitro studies and clinical trials.

AUTHOR CONTRIBUTIONS

Gozde Basara: Conceptualization; data curation; formal analysis; methodology; visualization; writing—original draft; writing—review & editing. **Lara Ece Celebi**: Data curation; formal analysis; methodology; visualization; writing—original draft; writing—review & editing. **George Ronan**: Methodology; writing—original draft. **Victoria Discua Santos**: Data curation; writing—original draft. **Pinar Zorlutuna**: Conceptualization; funding acquisition; project administration; resources; supervision; writing—original draft; writing—review & editing.

ACKNOWLEDGMENTS

This work was supported by NIH Award #1 R01 HL141909-01A1 and NSF-CAREER Award # 1651385. Our supporting sources were not involved in study design for this publication.

CONFLICT OF INTEREST STATEMENT

The authors declare no conflict of interest.

DATA AVAILABILITY STATEMENT

The raw/processed data required to reproduce these results can be provided upon reasonable request.

ETHICS STATEMENT

This study followed the Declaration of Helsinki guidelines. Institutional Review Board approval was waived for this study, as the Research Compliance team at the University of Notre Dame does not classify our research as human subject research given that the Indiana Donor Network refrains from providing any identifying information about the samples to researchers.

TRANSPARENCY STATEMENT

The lead author Pinar Zorlutuna affirms that this manuscript is an honest, accurate, and transparent account of the study being reported; that no important aspects of the study have been omitted; and that any discrepancies from the study as planned (and, if relevant, registered) have been explained.

ORCID

Pinar Zorlutuna http://orcid.org/0000-0002-3122-7553

REFERENCES

1. Tsao CW, Aday AW, Almarzooq ZI, et al. Heart disease and stroke statistics—2022 update: a report from the American Heart Association. *Circulation*. 2022;145:e153-e639.
2. Khalil NN, McCain ML. Engineering the cellular microenvironment of post-infarct myocardium on a chip. *Front Cardiovasc Med*. 2021;8:709871. doi:10.3389/fcvm.2021.709871

3. Frangogiannis N. Targeting the inflammatory response in healing myocardial infarcts. *Curr Med Chem*. 2006;13:1877-1893.
4. Virag JI, Murry CE. Myofibroblast and endothelial cell proliferation during murine myocardial infarct repair. *Am J Pathol*. 2003;163:2433-2440.
5. Torabi A, Cleland JGF, Khan NK, et al. The timing of development and subsequent clinical course of heart failure after a myocardial infarction. *Eur Heart J*. 2008;29:859-870.
6. Murphy G, Reynolds JJ. Extracellular matrix degradation. In: Royce PM, Steinmann B, eds. *Connective Tissue and Its Heritable Disorders: Molecular, Genetic, and Medical Aspects*, 2002:343-384.
7. Biernacka A, Frangogiannis NG. Aging and cardiac fibrosis. *Aging Dis*. 2011;2:158-173.
8. Ozcebe SG, Bahcecioglu G, Yue XS, Zorlutuna P. Effect of cellular and ECM aging on human iPSC-derived cardiomyocyte performance, maturity and senescence. *Biomaterials*. 2021;268:120554.
9. Acun A, Nguyen TD, Zorlutuna P. In vitro aged, hiPSC-origin engineered heart tissue models with age-dependent functional deterioration to study myocardial infarction. *Acta Biomater*. 2019;94:372-391.
10. Mastikhina O, Moon B-U, Williams K, et al. Human cardiac fibrosis-on-a-chip model recapitulates disease hallmarks and can serve as a platform for drug testing. *Biomaterials*. 2020;233:119741. doi:10.1016/j.biomaterials.2019.119741
11. Basara G, Bahcecioglu G, Ozcebe SG, Ellis BW, Ronan G, Zorlutuna P. Myocardial infarction from a tissue engineering and regenerative medicine point of view: a comprehensive review on models and treatments. *Biophys Rev*. 2022;3:031305. doi:10.1063/5.0093399
12. Yang Y, Lei D, Huang S, et al. Elastic 3D-printed hybrid polymeric scaffold improves cardiac remodeling after myocardial infarction. *Adv Healthc Mater*. 2019;8:1900065. doi:10.1002/adhm.201900065
13. Gao L, Kupfer ME, Jung JP, et al. Myocardial tissue engineering with cells derived from human-induced pluripotent stem cells and a native-like, high-resolution, 3-dimensionally printed scaffold. *Circ Res*. 2017;120:1318-1325.
14. Chang SC, Ren S, Rau CD, Wang JJ. Isoproterenol-induced heart failure mouse model using osmotic pump implantation. In: Ishikawa K, ed. *Experimental models of cardiovascular diseases: Methods and protocols*. Humana Press Inc.; 2018:207-220.
15. Duran JM, Taghavi S, Berretta RM, et al. A characterization and targeting of the infarct border zone in a swine model of myocardial infarction. *Clin Transl Sci*. 2012;5:416-421. doi:10.1111/j.1752-8062.2012.00432.x
16. Seguret M, Vermersch E, Jouve C, Hulot J-S. Cardiac organoids to model and heal heart failure and cardiomyopathies. *Biomedicines*. 2021;9:563. doi:10.3390/biomedicines9050563
17. House A, Atalla I, Lee EJ, Guvendiren M. Designing biomaterial platforms for cardiac tissue and disease modeling. *Advanced NanoBiomed Research*. 2021;1:2000022. doi:10.1002/anbr.202000022
18. Picchio V, Floris E, Derevyanchuk Y, et al. Multicellular 3D models for the study of cardiac fibrosis. *Int J Mol Sci*. 2022;23:11642. doi:10.3390/ijms231911642
19. Richardson W, Clarke S, Quinn T, Holmes J. Physiological implications of myocardial scar structure. *Compr. Physiol*. 2015;5:1877-1909. doi:10.1002/cphy.c140067
20. Alonzo M, El Khoury R, Nagiah N, Thakur V, Chattopadhyay M, Joddar B. 3D biofabrication of a cardiac tissue construct for sustained longevity and function. *ACS Appl Mater Interfaces*. 2022;14:21800-21813. doi:10.1021/acsami.1c23883
21. Koti P, Muselimyan N, Mirdamadi E, Asfour H, Sarvazyan NA. Use of GelMA for 3D printing of cardiac myocytes and fibroblasts. *J 3D Print Med*. 2019;3:11-22. doi:10.2217/3dp-2018-0017
22. Basara G, Ozcebe SG, Ellis BW, Zorlutuna P. Tunable human myocardium derived decellularized extracellular matrix for 3D bioprinting and cardiac tissue engineering. *Gels*. 2021;7:70. doi:10.3390/gels7020070
23. García-Lizarribar A, Fernández-Garibay X, Velasco-Mallorquí F, Castaño AG, Samitier J, Ramon-Azcon J. Composite biomaterials as long-lasting scaffolds for 3D bioprinting of highly aligned muscle tissue. *Macromol Biosci*. 2018;18:1800167.
24. Kang LH, Armstrong PA, Lee LJ, Duan B, Kang KH, Butcher JT. Optimizing photo-encapsulation viability of heart valve cell types in 3D printable composite hydrogels. *Ann Biomed Eng*. 2017;45:360-377.
25. Yue K, Trujillo-de Santiago G, Alvarez MM, Tamayol A, Annabi N, Khademhosseini A. Synthesis, properties, and biomedical applications of gelatin methacryloyl (GelMA) hydrogels. *Biomaterials*. 2015;73:254-271.
26. Basara G, Yue X, Zorlutuna P. Dual crosslinked gelatin methacryloyl hydrogels for photolithography and 3D printing. *Gels*. 2019;5:34. doi:10.3390/gels5030034
27. Poldervaart MT, Goversen B, De Ruijter M, et al. 3D bioprinting of methacrylated hyaluronic acid (MeHA) hydrogel with intrinsic osteogenicity. *PLoS One*. 2017;12:e0177628.
28. Skardal A, Zhang J, McCoard L, Xu X, Oottamasathien S, Prestwich GD. Photocrosslinkable hyaluronan-gelatin hydrogels for two-step bioprinting. *Tissue Eng Part A*. 2010;16:2675-2685.
29. Gil-Cabrerizo P, Saludas L, Prósper F, et al. Development of an injectable alginate-collagen hydrogel for cardiac delivery of extracellular vesicles. *Int J Pharm*. 2022;629:122356.
30. Yáñez-Mó M, Siljander PR-M, Andreu Z, et al. Biological properties of extracellular vesicles and their physiological functions. *J Extracell Vesicles*. 2015;4:27066. doi:10.3402/jev.v4.27066
31. Xu M, Ye Z, Song X, Huang R. Differences in the cargos and functions of exosomes derived from six cardiac cell types: a systematic review. *Stem Cell Res Ther*. 2019;10:194. doi:10.1186/s13287-019-1297-7
32. Ren X, Ellis BW, Ronan G, et al. A multiplexed ion-exchange membrane-based miRNA (MIX·miR) detection platform for rapid diagnosis of myocardial infarction. *Lab Chip*. 2021;21:3876-3887. doi:10.1039/D1LC00685A
33. Huang L, Ma W, Ma Y, Feng D, Chen H, Cai B. Exosomes in mesenchymal stem cells, a new therapeutic strategy for cardiovascular diseases? *Int J Biol Sci*. 2015;11:238-245. doi:10.7150/ijbs.10725
34. Huang K, Ozpinar EW, Su T, et al. An off-the-shelf artificial cardiac patch improves cardiac repair after myocardial infarction in rats and pigs. *Sci Transl Med*. 2020;12:eaat9683. doi:10.1126/scitranslmed.aat9683
35. Traverse JH, Henry TD, Dib N, et al. First-in-man study of a cardiac extracellular matrix hydrogel in early and late myocardial infarction patients. *JACC Basic Transl Sci*. 2019;4:659-669. doi:10.1016/j.jacbts.2019.07.012
36. Arslan U, Moruzzi A, Nowacka J, et al. Microphysiological stem cell models of the human heart. *Mater Today. Bio*. 2022;14:100259. doi:10.1016/j.mtbio.2022.100259
37. Reilly L, Munawar S, Zhang J, Crone WC, Eckhardt LL. Challenges and innovation: disease modeling using human-induced pluripotent stem cell-derived cardiomyocytes. *Front Cardiovasc Med*. 2022;9:966094. doi:10.3389/fcvm.2022.966094
38. Ellis BW, Acun A, Can UI, Zorlutuna P. Human iPSC-derived myocardium-on-chip with capillary-like flow for personalized medicine. *Biomicrofluidics*. 2017;11:024105. doi:10.1063/1.4978468
39. Wanjare M, Kawamura M, Hu C, et al. Vascularization of engineered spatially patterned myocardial tissue derived from human pluripotent stem cells in vivo. *Front Bioeng Biotechnol*. 2019;7. doi:10.3389/fbioe.2019.00208

40. Yue X, Acun A, Zorlutuna P. Transcriptome profiling of 3D co-cultured cardiomyocytes and endothelial cells under oxidative stress using a photocrosslinkable hydrogel system. *Acta Biomater*. 2017;58:337-348. doi:10.1016/j.actbio.2017.06.031
41. Ellis BW, Ronan G, Ren X, et al. Human heart anoxia and reperfusion tissue (HEART) model for the rapid study of exosome bound miRNA expression as biomarkers for myocardial infarction. *Small*. 2022;18:e2201330. doi:10.1002/smll.202201330
42. Giacomelli E, Meraviglia V, Campostrini G, et al. Human-iPSC-derived cardiac stromal cells enhance maturation in 3D cardiac microtissues and reveal non-cardiomyocyte contributions to heart disease. *Cell Stem Cell*. 2020;26:862-879. doi:10.1016/j.stem.2020.05.004
43. Kahn-Krell A, Pretorius D, Guragain B, et al. A three-dimensional culture system for generating cardiac spheroids composed of cardiomyocytes, endothelial cells, smooth-muscle cells, and cardiac fibroblasts derived from human induced-pluripotent stem cells. *Front Bioeng Biotechnol*. 2022;10:908848. doi:10.3389/fbioe.2022.908848
44. Zhao M, Tang Y, Zhou Y, Zhang J. Deciphering role of Wnt signalling in cardiac mesoderm and cardiomyocyte differentiation from human iPSCs: four-dimensional control of Wnt pathway for hiPSC-CMs differentiation. *Sci Rep*. 2019;9:19389. doi:10.1038/s41598-019-55620-x
45. Zhang J, Tao R, Campbell KF, et al. Functional cardiac fibroblasts derived from human pluripotent stem cells via second heart field progenitors. *Nat Commun*. 2019;10:2238. doi:10.1038/s41467-019-09831-5
46. Patsch C, Challet-Meylan L, Thoma EC, et al. Generation of vascular endothelial and smooth muscle cells from human pluripotent stem cells. *Nature Cell Biol*. 2015;17:994-1003. doi:10.1038/ncb3205
47. Nichol JW, Koshy ST, Bae H, Hwang CM, Yamanlar S, Khademhosseini A. Cell-laden microengineered gelatin methacrylate hydrogels. *Biomaterials*. 2010;31:5536-5544. doi:10.1016/j.biomaterials.2010.03.064
48. Hachet E, Van Den Berghe H, Bayma E, Block MR, Auzély-Velty R. Design of biomimetic cell-interactive substrates using hyaluronic acid hydrogels with tunable mechanical properties. *Biomacromolecules*. 2012;13:1818-1827. doi:10.1021/bm300324m
49. Nagaraju CK, Dries E, Popovic N, et al. Global fibroblast activation throughout the left ventricle but localized fibrosis after myocardial infarction. *Sci Rep*. 2017;7:10801. doi:10.1038/s41598-017-09790-1
50. Huebsch N, Loskill P, Mandegar MA, et al. Automated video-based analysis of contractility and calcium flux in human-induced pluripotent stem cell-derived cardiomyocytes cultured over different spatial scales. *Tissue Eng Part C Methods*. 2015;21:467-479. doi:10.1089/ten.tec.2014.0283
51. Balbi C, Vassalli G. Exosomes: beyond stem cells for cardiac protection and repair. *Stem Cells*. 2020;38:1387-1399. doi:10.1002/stem.3261
52. Wang AYL. Human induced pluripotent stem cell-derived exosomes as a new therapeutic strategy for various diseases. *Int J Mol Sci*. 2021;22:1769. doi:10.3390/ijms22041769
53. Yang PC. Induced pluripotent stem cell (iPSC)–derived exosomes for precision medicine in heart failure. *Circ Res*. 2018;122:661-663. doi:10.1161/CIRCRESAHA.118.312657
54. Gavard J. Endothelial permeability and VE-cadherin. *Cell Adh Migr*. 2014;8:158-164. doi:10.4161/cam.29026
55. Wang EY, Rafatian N, Zhao Y, et al. Biowire model of interstitial and focal cardiac fibrosis. *ACS Cent Sci*. 2019;5:1146-1158. doi:10.1021/acscentsci.9b00052
56. Richards DJ, Li Y, Kerr CM, et al. Human cardiac organoids for the modelling of myocardial infarction and drug cardiotoxicity. *Nat Biomed Eng*. 2020;4:446-462. doi:10.1038/s41551-020-0539-4
57. Fedorovich NE, Oudshoorn MH, van Geemen D, Hennink WE, Alblas J, Dhert WJA. The effect of photopolymerization on stem cells embedded in hydrogels. *Biomaterials*. 2009;30:344-353. doi:10.1016/j.biomaterials.2008.09.037
58. Souders CA, Bowers SLK, Baudino TA. Cardiac fibroblast. *Circ Res*. 2009;105:1164-1176. doi:10.1161/CIRCRESAHA.109.209809
59. Williams CG, Malik AN, Kim TK, Manson PN, Elisseeff JH. Variable cytocompatibility of six cell lines with photoinitiators used for polymerizing hydrogels and cell encapsulation. *Biomaterials*. 2005;26:1211-1218. doi:10.1016/j.biomaterials.2004.04.024
60. Bonafè F, Govoni M, Giordano E, Caldarera CM, Guarnieri C, Muscari C. Hyaluronan and cardiac regeneration. *J Biomed Sci*. 2014;21:100. doi:10.1186/s12929-014-0100-4
61. Snider JC, Riley LA, Mallory NT, et al. Targeting 5-HT2B receptor signaling prevents border zone expansion and improves microstructural remodeling after myocardial infarction. *Circulation*. 2021;143:1317-1330. doi:10.1161/CIRCULATIONAHA.120.051517
62. Litviňuková M, Talavera-López C, Maatz H, et al. Cells of the adult human heart. *Nature*. 2020;588:466-472. doi:10.1038/s41586-020-2797-4
63. Venugopal H, Hanna A, Humeres C, Frangogiannis NG. Properties and functions of fibroblasts and myofibroblasts in myocardial infarction. *Cells*. 2022;11:1386. doi:10.3390/cells11091386
64. Kung GL, Vaseghi M, Gahm JK, et al. Microstructural infarct border zone remodeling in the post-infarct swine heart measured by diffusion tensor MRI. *Front Physiol*. 2018;9. doi:10.3389/fphys.2018.00826
65. Noguchi R, Nakayama K, Itoh M, et al. Development of a three-dimensional pre-vascularized scaffold-free contractile cardiac patch for treating heart disease. *J Heart Lung Transplant*. 2016;35:137-145. doi:10.1016/j.healun.2015.06.001
66. Schroer AK, Merryman WD. Mechanobiology of myofibroblast adhesion in fibrotic cardiac disease. *J Cell Sci*. 2015;128:1865-1875. doi:10.1242/jcs.162891
67. King JH, Huang CLH, Fraser JA. Determinants of myocardial conduction velocity: implications for arrhythmogenesis. *Front Physiol*. 2013;4:154.
68. Fan X, Hughes BG, Ali MAM, Cho WJ, Lopez W, Schulz R. Dynamic alterations to α-actinin accompanying sarcomere disassembly and reassembly during cardiomyocyte mitosis. *PloS one*. 2015;10:e0129176. doi:10.1371/journal.pone.0129176
69. Vestweber D. VE-Cadherin. *Arterioscler Thromb Vasc Biol*. 2008;28:223-232. doi:10.1161/ATVBAHA.107.158014
70. Doppler SA, Carvalho C, Lahm H, et al. Cardiac fibroblasts: more than mechanical support. *J Thorac Dis*. 2017;9:S36-S51. doi:10.21037/jtd.2017.03.122
71. Frangogiannis N, Michael LH, Entman ML. Myofibroblasts in reperfused myocardial infarcts express the embryonic form of smooth muscle myosin heavy chain (SMemb). *Cardiovasc Res*. 2000;48:89-100. doi:10.1016/S0008-6363(00)00158-9
72. Nguyen DT, Nagarajan N, Zorlutuna P. Effect of substrate stiffness on mechanical coupling and force propagation at the infarct boundary. *Biophys J*. 2018;115:1966-1980. doi:10.1016/j.bpj.2018.08.050
73. Tallawi M, Rai R, Boccaccini AR, Aifantis KE. Effect of substrate mechanics on cardiomyocyte maturation and growth. *Tissue Eng Part B Rev*. 2015;21:157-165. doi:10.1089/ten.teb.2014.0383
74. Chen CW, Wang LL, Zaman S, et al. Sustained release of endothelial progenitor cell-derived extracellular vesicles from shear-thinning hydrogels improves angiogenesis and promotes function after myocardial infarction. *Cardiovasc Res*. 2018;114:1029-1040. doi:10.1093/cvr/cvy067
75. Liu J, He J, Liu J, et al. Rapid 3D bioprinting of in vitro cardiac tissue models using human embryonic stem cell-derived cardiomyocytes.

Bioprinting Amst. Neth. 2019;13:e00040. doi:10.1016/j.bprint.2019.e00040
76. Miller KL, Xiang Y, Yu C, et al. Rapid 3D Bioprinting of a human iPSC-derived cardiac micro-tissue for high-throughput drug testing. *Organs-on-a-Chip*. 2021;3:100007. doi:10.1016/j.ooc.2021.100007
77. Basara G, Bahcecioglu G, Ren X, Zorlutuna P. An experimental and numerical investigation of cardiac tissue-patch interrelation. *J Biomech Eng*. 2023;145:081004. doi:10.1115/1.4062736
78. Ronan G, Bahcecioglu G, Yang J, Zorlutuna P. Age and sex-dependent differences in human cardiac matrix-bound exosomes modulate fibrosis through synergistic miRNA effects. *bioRxiv*. Preprint posted online 2022. doi:10.1101/2022.11.14.516464

SUPPORTING INFORMATION

Additional supporting information can be found online in the Supporting Information section at the end of this article.

How to cite this article: Basara G, Celebi LE, Ronan G, Discua Santos V, Zorlutuna P. 3D bioprinted aged human post-infarct myocardium tissue model. *Health Sci Rep*. 2024;7:e1945. doi:10.1002/hsr2.1945